AFRL-AFOSR-UK-TR-2019-0051

Forward Scattering Effect Exploitation in Passive Radars

Krzysztof Kulpa
POLITECHNIKA WARSZAWSKA
1 PLAC POLITECHNIKI
WARSZAWA, MAZOWIECKIE, 00-661
PL

09/12/2019
Final Report

Air Force Research Laboratory
Air Force Office of Scientific Research
European Office of Aerospace Research and Development
Unit 4515 Box 14, APO AE 09421

REPORT DOCUMENTATION PAGE	*Form Approved* *OMB No. 0704-0188*

1. REPORT DATE *(DD-MM-YYYY)* 12-09-2019	**2. REPORT TYPE** Final	**3. DATES COVERED** *(From - To)* 15 Jan 2017 to 14 Jan 2019

4. TITLE AND SUBTITLE Forward Scattering Effect Exploitation in Passive Radars	**5a. CONTRACT NUMBER**
	5b. GRANT NUMBER FA9550-17-1-0041
	5c. PROGRAM ELEMENT NUMBER 61102F
6. AUTHOR(S) Krzysztof Kulpa	**5d. PROJECT NUMBER**
	5e. TASK NUMBER
	5f. WORK UNIT NUMBER
7. PERFORMING ORGANIZATION NAME(S) AND ADDRESS(ES) POLITECHNIKA WARSZAWSKA 1 PLAC POLITECHNIKI WARSZAWA, MAZOWIECKIE, 00-661 PL	**8. PERFORMING ORGANIZATION REPORT NUMBER**
9. SPONSORING/MONITORING AGENCY NAME(S) AND ADDRESS(ES) EOARD Unit 4515 APO AE 09421-4515	**10. SPONSOR/MONITOR'S ACRONYM(S)** AFRL/AFOSR IOE
	11. SPONSOR/MONITOR'S REPORT NUMBER(S) AFRL-AFOSR-UK-TR-2019-0051

12. DISTRIBUTION/AVAILABILITY STATEMENT
A DISTRIBUTION UNLIMITED: PB Public Release

13. SUPPLEMENTARY NOTES

14. ABSTRACT
Recreated existing theory related to bi-static radar reflections from targets and noise. The Grant options were not exercised as a result.

15. SUBJECT TERMS
passive radar, backscatter radar, measured bistatic range and velocity

16. SECURITY CLASSIFICATION OF:			**17. LIMITATION OF ABSTRACT**	**18. NUMBER OF PAGES**	**19a. NAME OF RESPONSIBLE PERSON** LOCKWOOD, NATHANIEL
a. REPORT	**b. ABSTRACT**	**c. THIS PAGE**			
Unclassified	Unclassified	Unclassified	SAR		**19b. TELEPHONE NUMBER** *(Include area code)* 011-44-1895-616005

Standard Form 298 (Rev. 8/98)
Prescribed by ANSI Std. Z39.18

Warsaw University of Technology

Research Report

Forward Scattering Effect Exploitation in Passive Radars

Final Report

Authors:

Krzysztof Kulpa
Piotr Samczyński
Piotr Krysik
Bartlomiej Salski
Paweł Kopyt
Marta Malik

Warsaw, Poland, April 11, 2018

This material is based upon work supported by the Air Force Office of Scientific Research, Air Force Material Command, USAF under Award No. FA9550-17-1-0041.

Contents

Any opinions, findings, and conclusions or recommendations expressed in this publication are those of the authors and do not necessarily reflect the views of the Air Force Office of Scientific Research, Air Force Materiel Command, USAF.

This material is based upon work supported by the Air Force Office of Scientific Research, Air Force Material Command, USAF under Award No. FA9550-17-1-0041.

1. Introduction

Objective of the research is to develop new methods suitable for forward scattering exploitation in a passive radar. While an effective radar cross-section in a forward scattering geometry is much higher than in a backscattering region, the forward scattering gives us an opportunity to use the passive radars for detecting small objects. However, a disadvantage of the forward scattering geometry is that its bistatic range (defined as difference of the direct path length and target-reflected path length) is much smaller than the actual distance to the target. In addition, the bistatic velocity is very low; in fact, much lower than the real target velocity. As a result the effective range and velocity resolutions of the passive radar are reduced. Also, the ability to exploit the forward scattering effect is typically limited by the direct signal suppression (CLEAN) algorithm. Most methods used to deal with issues concerning the direct signal suppression reduce also an amplitude of the desired echoes with a small angular separation from a transmitter, thus degrading the usefulness of forward scattering measurements.

The goal of this research will be accomplished by the following actions:

1. Conducting a study on the forward scattering phenomenon in the frequency bands suitable for passive radar (up to 1 GHz).
2. Conducting a study on the properties of the target echo in the forward scattering region.
3. Analyzing the applicability of various scenarios.

During the first year of contract execution the research was focused on two main subjects: fundamentals of the forwards scattering effect and simulations of the radar cross-section in the forward scattering region for selected shapes of the target.

2. Forward Scattering Phenomena

In the early days a majority of radar systems worked in bistatic configurations characterized by a displacement of the receiver's position in relation to a transmitter. Many of them were forward-scatter radar fences that warned about objects crossing the transmitter-receiver lines. German Klein Heidelberg bistatic radar system, was an example of such system with the forward scatter mode, and also it was the very first known operational hitchhiking radar [5].

Along with maturing of radiolocation as the field of knowledge, the operational radar systems were mostly built by radars with collocated transmitters and receivers (monostatic radar) that could observe electromagnetic waves backscattered from the objects. Reasons why the bistatic radar did not settle well were mainly related to its higher operational costs of separate transmitting and receiving sites and its greater complexity of the target's detection and localization. Currently, a resurgence of interest in the radars working with the bistatic geometry is observed mainly due to an ongoing development of Passive Coherent Location systems that typically work in such configurations. Also, there are high hopes that the bistatic radar capable of observing the electromagnetic wave scattered from the target in other directions than back to the transmitter would be able to detect stealth objects that by design should be undetectable by the monostatic radars.

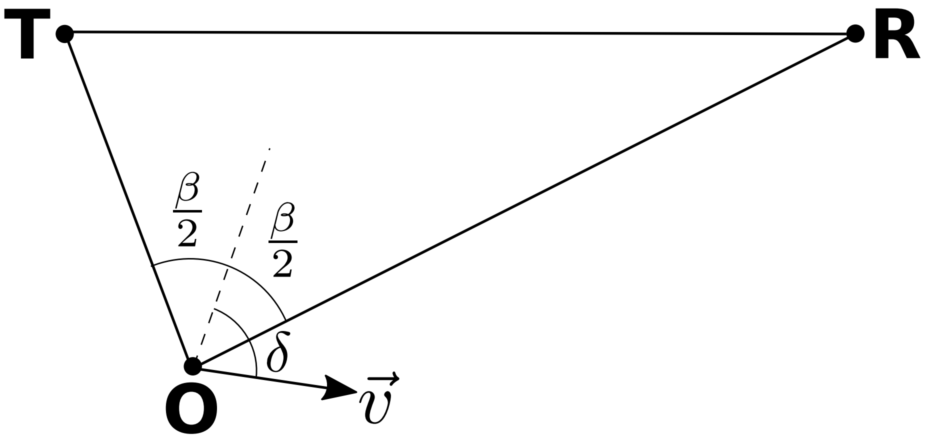

Figure 1 Bistatic geometry.

A bistatic radar geometry is shown in Figure 1. It is described by a bistatic triangle with vertices located at positions of transmitter *T*, receiver *R* and observed target *O*. The target is situated at the range $|TO|$ from the transmitter and the range $|OR|$ from the receiver. An angle β between $|TO|$ and $|OR|$ sides of the bistatic triangle is called the bistatic angle. Typically, the bistatic radar measures a time-difference between a transmitted wave and a target echo and a frequency difference of the target echo caused by the Doppler effect. These measurements are transformed into estimates of the bistatic range $R_B=|TO|+|RT|$ and the bistatic velocity.

The resolution of bistatic range measurement is given by the following expression:

This material is based upon work supported by the Air Force Office of Scientific Research, Air Force Material Command, USAF under Award No. FA9550-17-1-0041.

$$\Delta R_B = \frac{\Delta R_M}{cos\left(\frac{\beta}{2}\right)} \qquad (1)$$
$$\Delta R_M = \frac{c}{2B}$$

where ΔR_M is the range resolution for monostatic configuration, c is the speed of light and B is transmitted signal's bandwidth. The bistatic velocity measurement resolution is inversely proportional to the targets' Doppler frequency measurement f_d:

$$f_d = \frac{2|\vec{v}|}{\lambda} cos(\delta) \cdot cos\left(\frac{\beta}{2}\right) \qquad (2)$$

The line of sight $|TR|$ between the transmitter and the receiver is called a baseline. For an object located on the baseline the bistatic angle β is equal to 180°. In this situation a size of range resolution cell is approaching infinity and an echo of the object with an arbitrary velocity has always 0 Doppler frequency shift f_d at the receiver side. Therefore, the radar is unable to measure the distance or speed of such targets. Despite these drawbacks the bistatic geometry with the bistatic angle β close to 180° (the forward scatter geometry) has a huge advantage which is so called a forward scatter effect – the physical phenomena causing enlarged radar cross-section (*RCS*) that mainly depends on the object's shadow area, and does not depend on a kind of material the target is made of.

It is worth mentioning that with an application of signal processing algorithms tailored for the forward scatter radar (FSR), it is possible to find a position of the object together with its velocity and angle at which it crosses the baseline [4]. However, such processing is more sophisticated and computationally complex than the correlation processing typically applied in the bistatic radar, as it requires optimization with respect to multiple variables (velocity, point and angle of crossing the baseline). Also, it is usually assumed that the target has a constant velocity vector over the observation time that is several times longer than typical integration interval in the classical bistatic radar.

3. Forward Scatter Radar Cross-Section

The enhancement of target's RCS in the forward scatter region and hence its extended detection range is the main factor driving interest in FSR. The forward scatter effect is a result of co-phase perturbations of the waves in the object's shadow. These interferences cause focusing of the field on a line perpendicular to the target's shadow area.

In the optical region, when the target is significantly larger than the wavelength, the forward scatter RCS (FS RCS) can be quantitatively assessed by means of the approximation of physical optics theory. It is assumed that the target is located in a far field of the transmitting antenna, and that the receiving antenna is in another far field in respect to the target. To exclude an influence of the target's self scattering, it is also assumed that the target is a perfect black body. It should be noted however that for targets with dimensions significantly exceeding the wavelength, the impact of self-scattered field is much weaker in the shadow region (for β close to 180°) than the impact of the shadow field itself.

In order to find the maximal expected FS RCS for the bistatic angle $\beta = 180°$ as well as its changes together with a roll-off of β, known from the optics, the Babinet's principle can be applied. It states that a diffraction pattern from an opaque body is identical to the one from a hole of the same size and shape, except for the overall forward beam intensity (Figure 2).

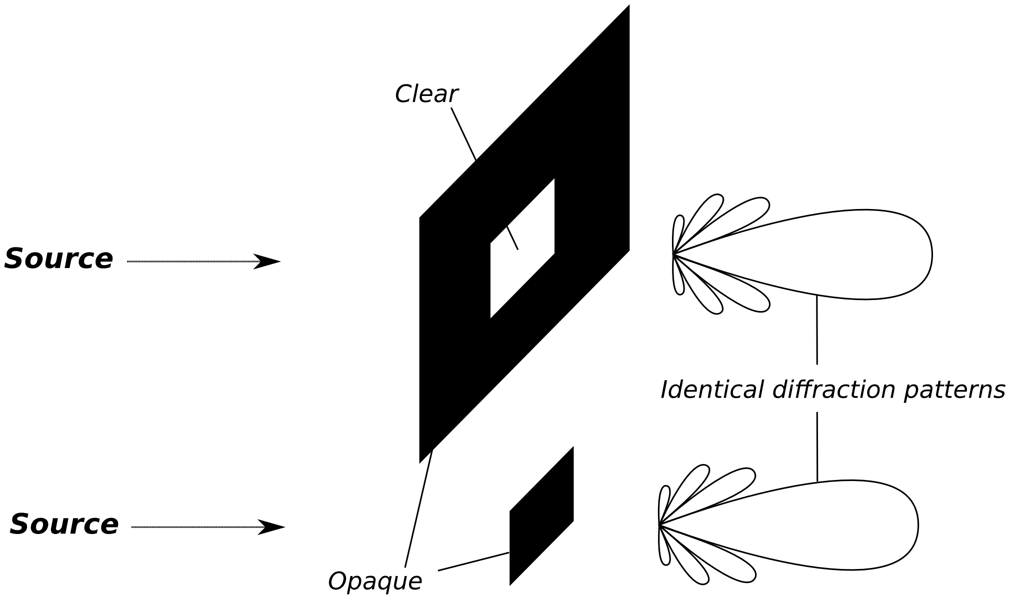

Figure 2. Illustration of the Babinet's principle.

The application of optical approach to the analysis of the forward scatter effect does not consider an electromagnetic wave polarization. An extension of the Babinet's principle to the electromagnetic waves can be found in [1]. However, for the analysis of pattern of the forward scatter beam the optical approach is sufficient.

This material is based upon work supported by the Air Force Office of Scientific Research, Air Force Material Command, USAF under Award No. FA9550-17-1-0041.

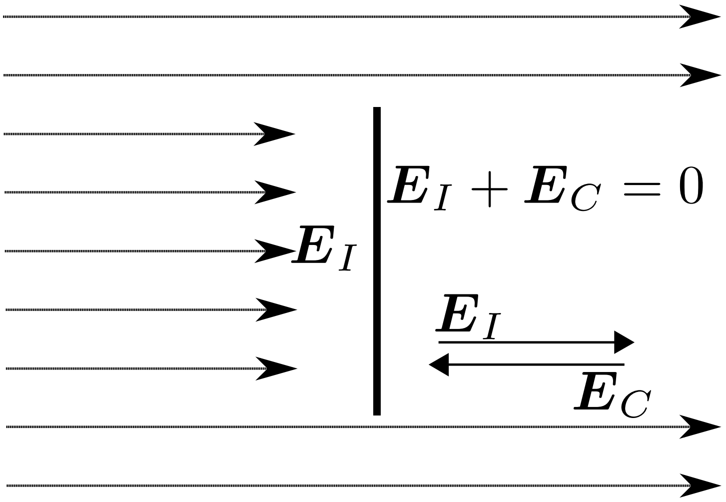

Figure 3. Shadow 'radiation'.

Let us consider a black body (absorbing object) of a size much larger than the wavelength that is located in a way of the plane wave (Figure 3) [2]. In a vicinity of the illuminated plane’s side an intensity of the electric field is equal to E_I. Just behind of the absorbing object, with respect to the wave source, a shadow region is formed with the intensity of the electric field equal to zero. This situation can be described mathematically with use of a compensating field with intensity E_C that cancels the field on the illuminated side. Therefore, E_C has the same amplitude and reversed sign in relation to the intensity E_I of the field of the incident wave:

$$\begin{aligned} E_I + E_C &= 0 \\ E_C &= -E_I \end{aligned} \quad (3)$$

Significant implication of that observation is that a shadow area of the object acts as an antenna aperture that is source a wave with electric intensity E_C. In the far field of the shadow 'radiation' a cross section is determined by an area of projection of the target shadow contour onto a plane perpendicular to a direction of the propagation of the incident wave; and it is independent of its three dimensional shape or the material’s type of its coating.

For the bistatic angle β=180°, in the far field of 'radiation' of the object with shadow (or silhouette) area S_A, the forward scatter RCS is determined by the following expression [3]:

$$\sigma_F(\beta = 180^\circ) = 4\pi\left(\frac{S_A}{\lambda}\right)^2. \quad (4)$$

The above equation can be rewritten as $\sigma_F(\beta=180^\circ) = G\, S_A$, where $G=4\pi S_A\,\lambda^2$ is a directive gain of the object in its shadow region. FS RCS is therefore G time larger than the shadow area S_A of the target and is usually significantly larger than the monostatic RCS for the optical region ($\lambda^2 \gg S_A$).

For a perfectly conducting sphere the monostatic RCS is equal to $\sigma_0(\beta=0^\circ) = \pi\, r^2$, where r is a diameter of the sphere, FS RCS of the sphere is G times larger. For example, for the sphere's diameter r=1 m and wavelength λ = 0.1 m the FS RCS is G_{dB} ≈ 26 dB larger than monostatic RCS.

An increase of the target RCS in the forward scatter region is known as the forward scatter effect that enables the radar to detect more distant targets than in the other bistatic configurations and also in monostatic configuration. Moreover, neither use of absorbing coating nor changing a 3D shape of the target does not prevent the target from being detected with the forward-scatter radar.

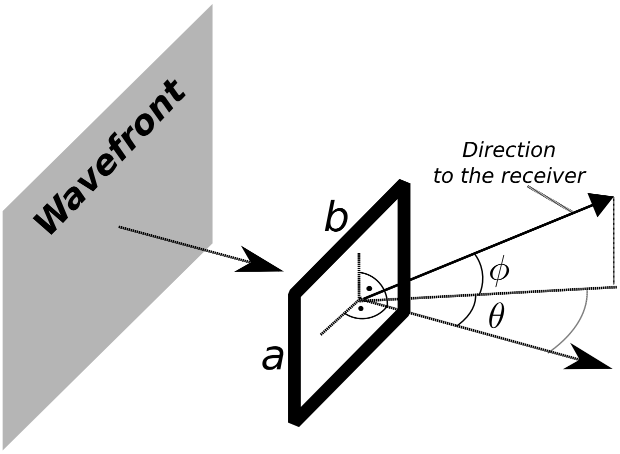

Figure 4. Scattering of a plane wave perpendicular to the rectangular target in direction.

The forward scatter 'radiation' of the target usually has a beam structure with a narrow main lobe inversely proportional to dimensions of the object's shadow area. For a rectangular target shown in Figure 4 the RCS observed by the distant receiver is described by the following expression [6]:

$$\sigma_F(\theta,\phi) = \frac{4\pi S_A^2}{\lambda^2} \cdot \left[\frac{sin\left(\frac{\pi a}{\lambda sin(\theta)}\right)}{\left(\frac{\pi a}{\lambda sin((\theta)}\right)}\right]^2 \cdot \left[\frac{sin\left(\frac{\pi b}{\lambda sin(\phi)}\right)}{\left(\frac{\pi b}{\lambda sin((\phi)}\right)}\right]^2 \tag{5}$$

where θ and ϕ are the angles defining a direction of the receiver in relation to the target with dimensions a and b. A peak value of the main lobe of the shadow 'radiation' is described by the Eq. (5), and its width in vertical and horizontal directions is inversely proportional to its a and b dimensions, respectively. The 3 dB width of the main lobe is approximately equal to:

$$\theta_{FS} \approx \frac{\lambda}{l} \tag{6}$$

For a square target with its side’s length equal 1 m and λ=0.1 m the main lobe’s width is approximately equal to 5.7°. The strongest influence of the forward scatter effect on the target's RCS is therefore observed for a small roll-off of the bistatic angle β from 180° only. However, an essential gain coming from the shadow 'radiation' over the self scattering of the object might remain in the side-lobes of the objects shadow pattern.

4. RCS Simulations

Angular scattering patterns presented in this report were calculated with a finite-difference time-domain (FDTD) method implemented in the QuickWave-3D (QW-3D) software package [7]. A computational model applied as shown in Figure 5 is surrounded by a Mur super-absorption, and contains a total-field/scattered-field (TF/SF) soft source (see a red contour in Figure 5), which is commonly used to excite a plane wave propagating at a given angle. If no obstacles are located inside the total-field area surrounded by the TF/SF source, there should be no electromagnetic field present in the scattered-field area beyond the TF/SF source. In that case, near-to-far field transform performed at a Huygens surface (see a green contour in Figure 5) located in the scattered-field area is expected to account only for the scattered field, which is of interest in this study.

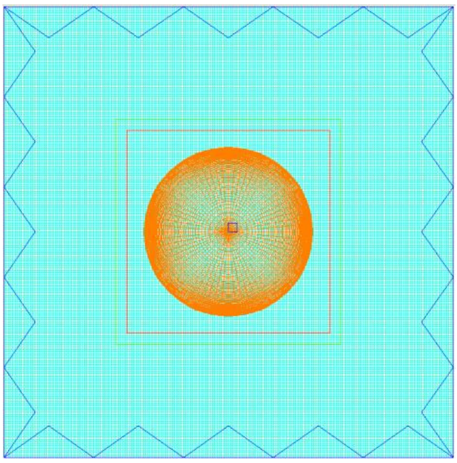

Figure 5. FDTD computational model.

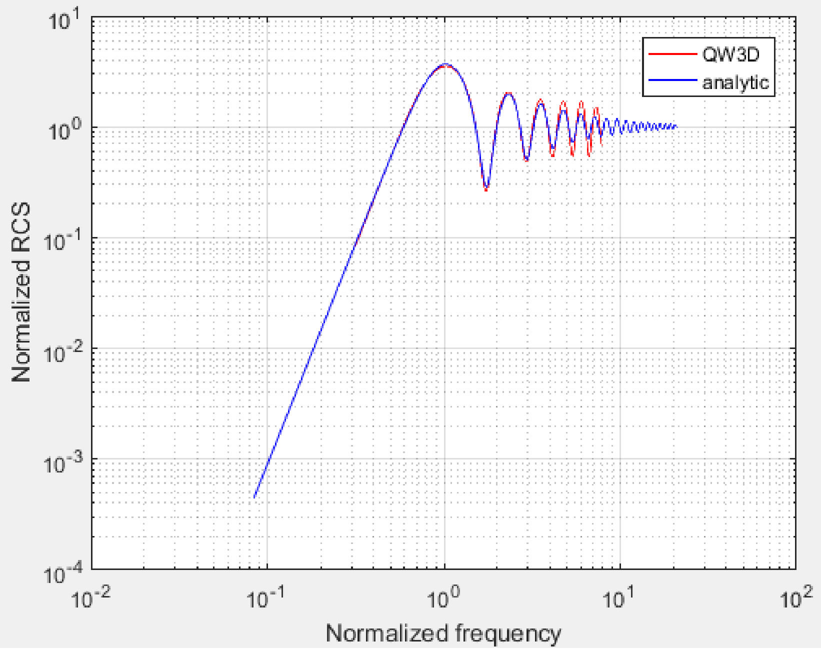

Figure 6. Spectrum of the normalized backward-scattered RCS of a metallic sphere.

This material is based upon work supported by the Air Force Office of Scientific Research, Air Force Material Command, USAF under Award No. FA9550-17-1-0041.

Radar cross-section (RCS) is calculated as follows:

$$RCS\ [dBsm] = 10\log(\frac{P_{scat}}{S_{inc}}) \quad (7)$$

where S_{inc} [W/m^2] stands for the surface power density of the incident plane wave, and P_{scat} [W] is the power scattered at a given angle, which can be calculated as follows:

$$P_{scat}\ [W] = P_{tot}\ D \quad (8)$$

where P_{tot} [W] represents total scattered power, and D is angular directivity of the scattered field.

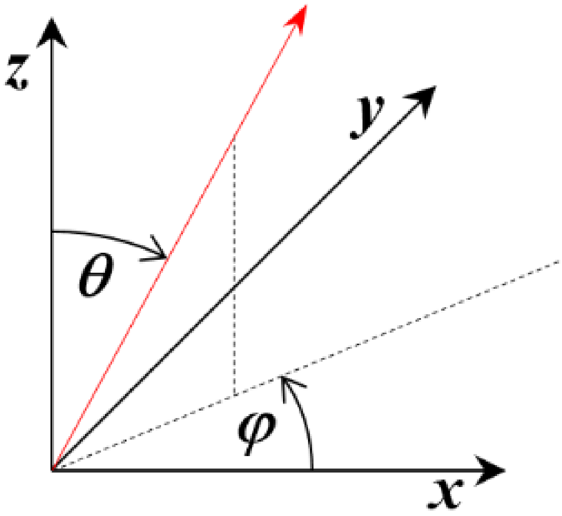

Figure 7. Spherical coordinate system.

As a starting point of the study presented hereafter, Figure 6 presents exemplary computational results of the normalized backward-scattered RCS of a metallic sphere computed with FDTD. A comparison of these results with the analytical solution [8] shows a proper conformity at moderate frequencies. An accuracy at the higher spectral range could be improved if finer FDTD meshing were applied to the model, however, at the cost of much larger computational effort.

Computational RCS results of various typical metallic objects, as presented below in this study, were calculated for the plane wave incident for a given object with a few angles specified in the spherical coordinate system, where φ (θ) is an azimuth (elevation) angle (see Figure 7).

4.1 A Metallic Sphere

At first, three-dimensional (3D) RCS of a metallic sphere illuminated at the xy-plane (φ, θ) = (0^0, 90^0) was calculated at various frequencies. It can be noticed in Figure 8 that at the frequencies lower than ca. $r/\lambda < 0.2$ (r – a sphere's radius, λ – a wavelength), the backward-

This material is based upon work supported by the Air Force Office of Scientific Research, Air Force Material Command, USAF under Award No. FA9550-17-1-0041.

scattering dominates in the whole scattering pattern, while for the higher frequencies the forward-scattering becomes substantially enhanced, which is related to the broadening of a shadow area behind the illuminated object.. It can be compared quantitatively in Figure 9, where RCSs of the sphere calculated in the E-plane (left) and H-plane (right) are presented. RCS angular maps shown in Figure 10 confirm that the largest achievable RCS in the whole frequency spectrum is the forward-scattered one. For instance, the forward to backward RCS ratio RCSf($r/\lambda = 0.5$) / RCSb($r/\lambda = 0.125$) is as large as 5. In addition, it is worth noting that at the Mie region (e.g. $r/\lambda = 0.25$ in Figure 10) a substantial scattering occurs also at directions orthogonal to the incidence path, while the backward-scattering is suppressed.

For the purpose of better understanding of the phenomenon of forward-scattering, an electromagnetic field distribution computed in the E-plane at $r/\lambda = 0.5$ is shown in Figure 11, with the incident beam propagating to the right. It can be noticed that in the total-field area the propagation of the beam is substantially REDUCED in the forward direction, leading to a shadow effect. However, a forward-scattered field visible in the scattered-field area becomes ENHANCED. It implies that strong forward RCS does not necessarily mean that the forward-scattered beam is large, but rather that its difference with respect to the original un-scattered beam is large. In case of the bi-static radars, a forward-scattering detection of the objects is always a challenge. However, that issue may be alleviated if forward-scattering RCS becomes strongly directional so that slight deviations of the target from the forward-scattering path may result in a substantial cross-correlation of the signals collected by the reference and surveillance antennae, thus, leading to the reduction of the dead zone.

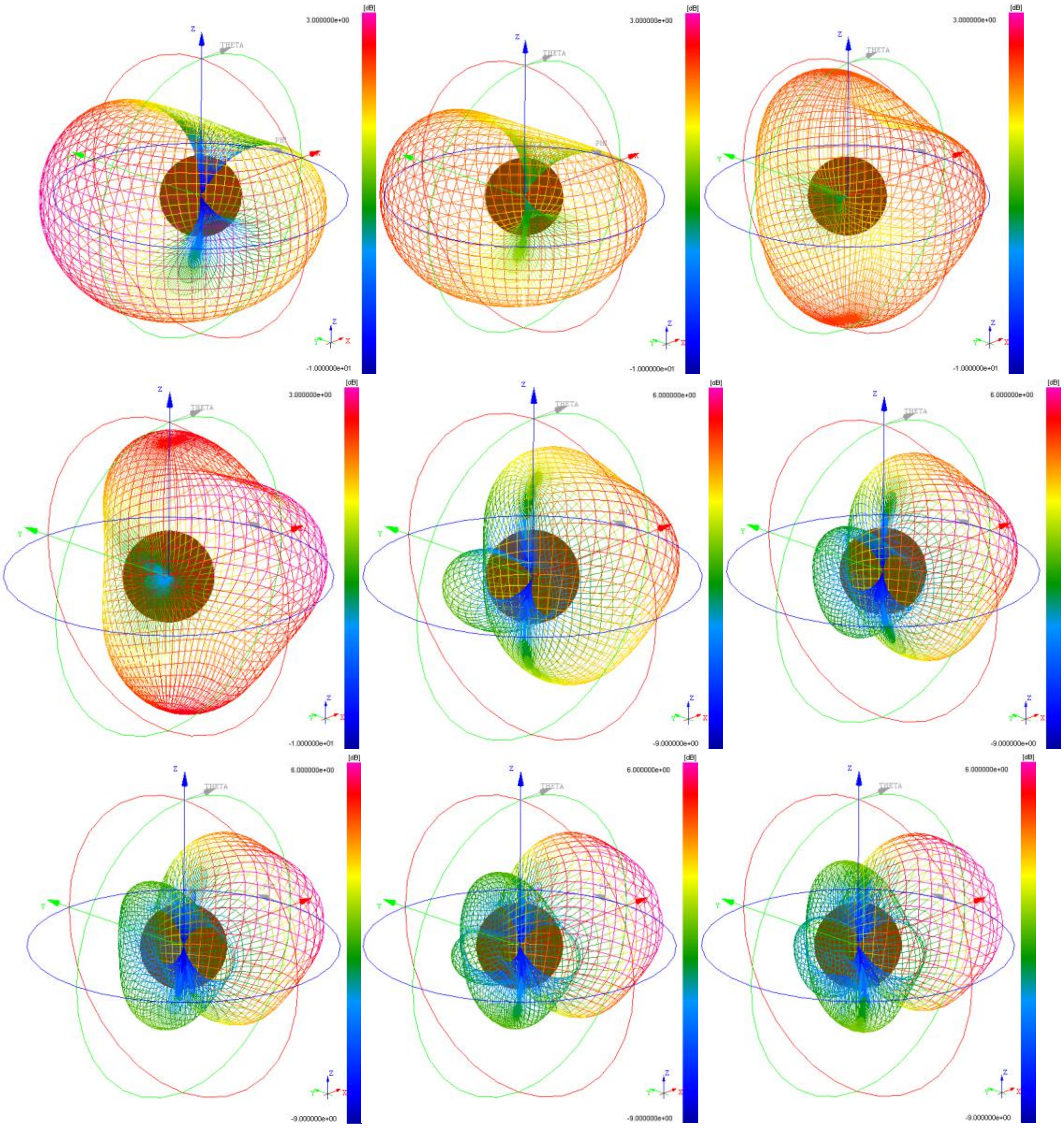

Figure 8. 3D RCS [dBsm] of a sphere (r = 18.75 cm) illuminated at (φ, θ) = (0^0, 90^0) for r/λ = [0.125, 0.1875, 0.25, 0.3125, 0.375, 0.4375, 0.5, 0.5625, 0.625].

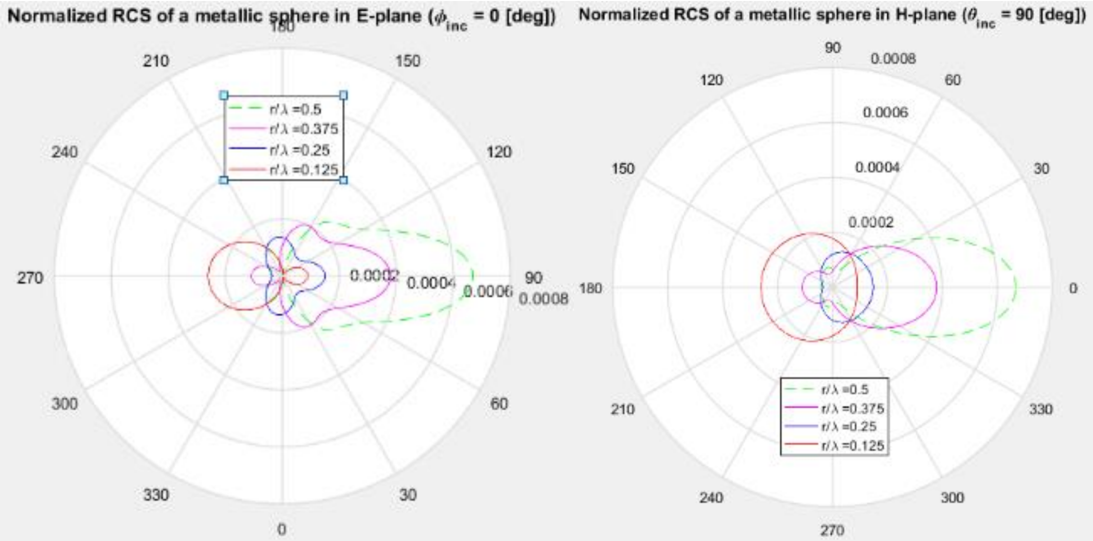

Figure 9. RCS in the E-plane (left) and H-plane (right) of a sphere (*r* = 18.75 cm) illuminated at (φ, θ) = (0^0, 90^0).

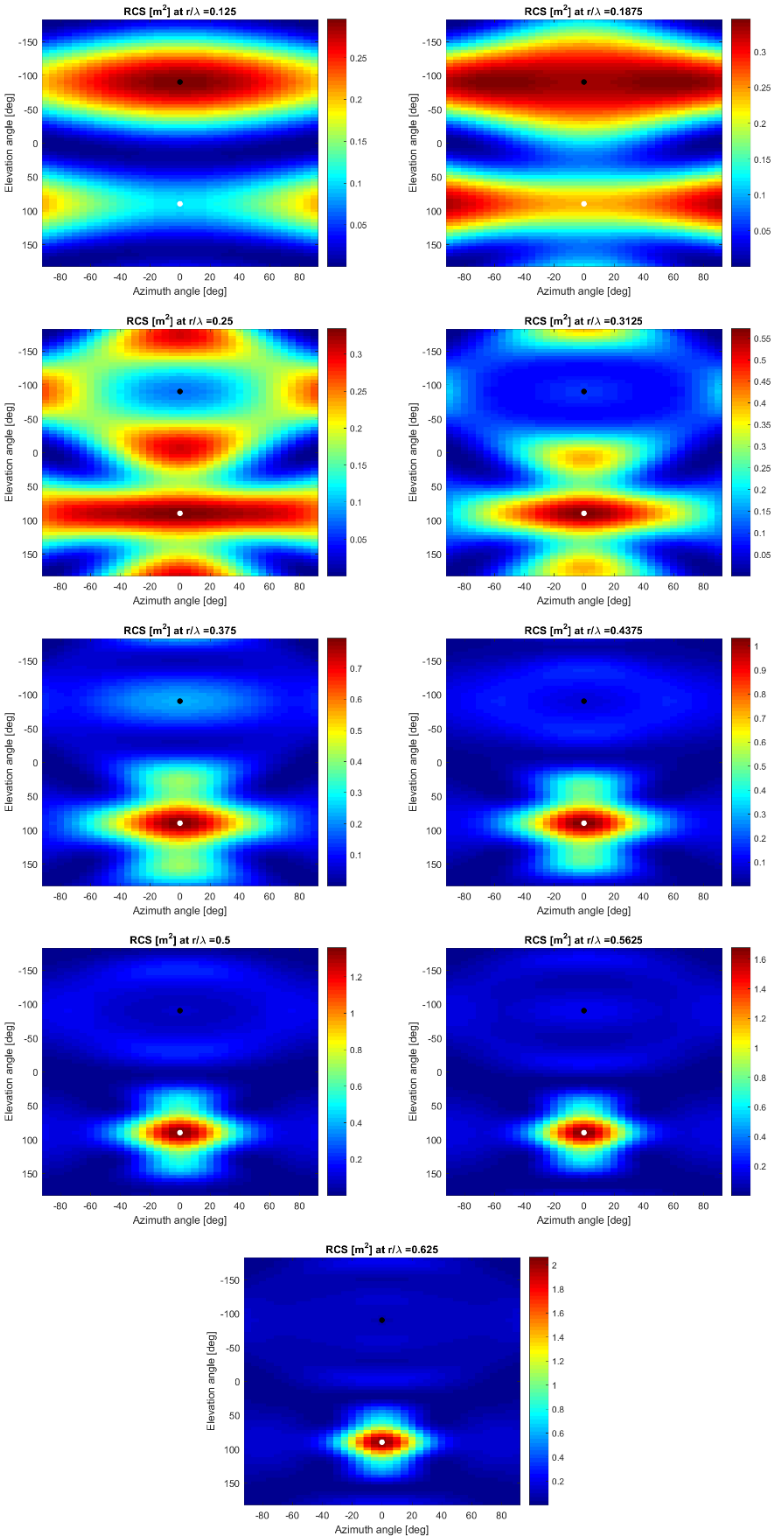

Figure 10. RCS map of a sphere (r = 18.75 cm) illuminated at (φ, θ) = (0^0, 90^0) (black dot – backward-scattering angle, white dot – forward-scattering angle).

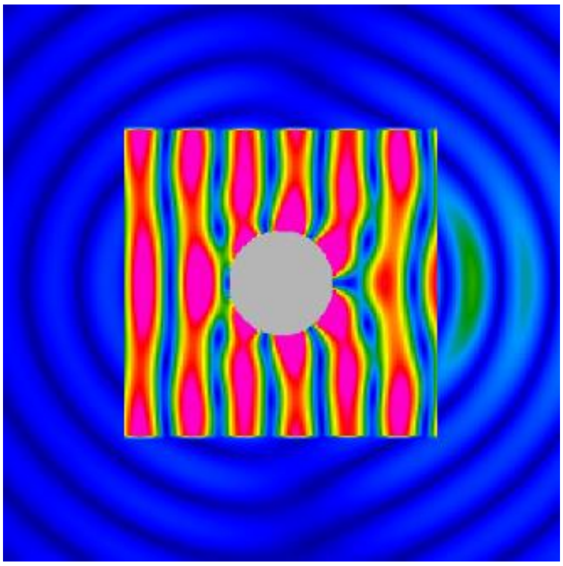

Figure 11. Electric field distribution at the E-plane of the metallic sphere computed at $r/\lambda = 0.5$.

4.2 A Metallic Cylinder

Another object under study here was a z-oriented metallic cylinder with various aspect ratios (L/2r). First, it can be noticed that the forward-scattering of the TE-polarized plane wave (an electric field polarized along the cylinder) illuminating a flat disc from its side profile (e.g. L/2r = 0.0625 in Figure 12) is slightly deflected from its forward path at the low frequencies as can be seen in Figure 12a. That phenomenon is not however observed for the TM polarization, which may be disadvantageous for the forward-scattering radars. Moreover, a comparison of Figure 12A and 12B shows that RCS for the TM polarization is at least 50 times stronger. As the frequency increases, the forward-scattering increases as well and becomes more focused at a forward angle, irrespective of polarization. As the elevation angle of the incidence is changing from a side illumination of the flat cylinder toward a top one of the flat cylinder, a specular scattering (a reflection from the cylinder bottom) is getting more enhanced, and also, both forward- and specular-scattering become more omnidirectional at an azimuth plane. However, for L/2r > 0.25 the low-frequency forward-scattering for the cylinder illuminated from the top is substantially diminished. The increase of the aspect ratio of the metallic cylinder leads to the increase of the backward-scattering that reaches its maximum for L/2r = 1, and then, relatively decreases again for long cylinders. It can also be noticed that such cylinders the scattering becomes more omnidirectional at the azimuth plane.

In case of the normal incidence of the wave onto electrically-long cylinders, several scattering side lobes distributed in the elevation plane occur, with their widths decreasing with the frequency.

This material is based upon work supported by the Air Force Office of Scientific Research, Air Force Material Command, USAF under Award No. FA9550-17-1-0041.

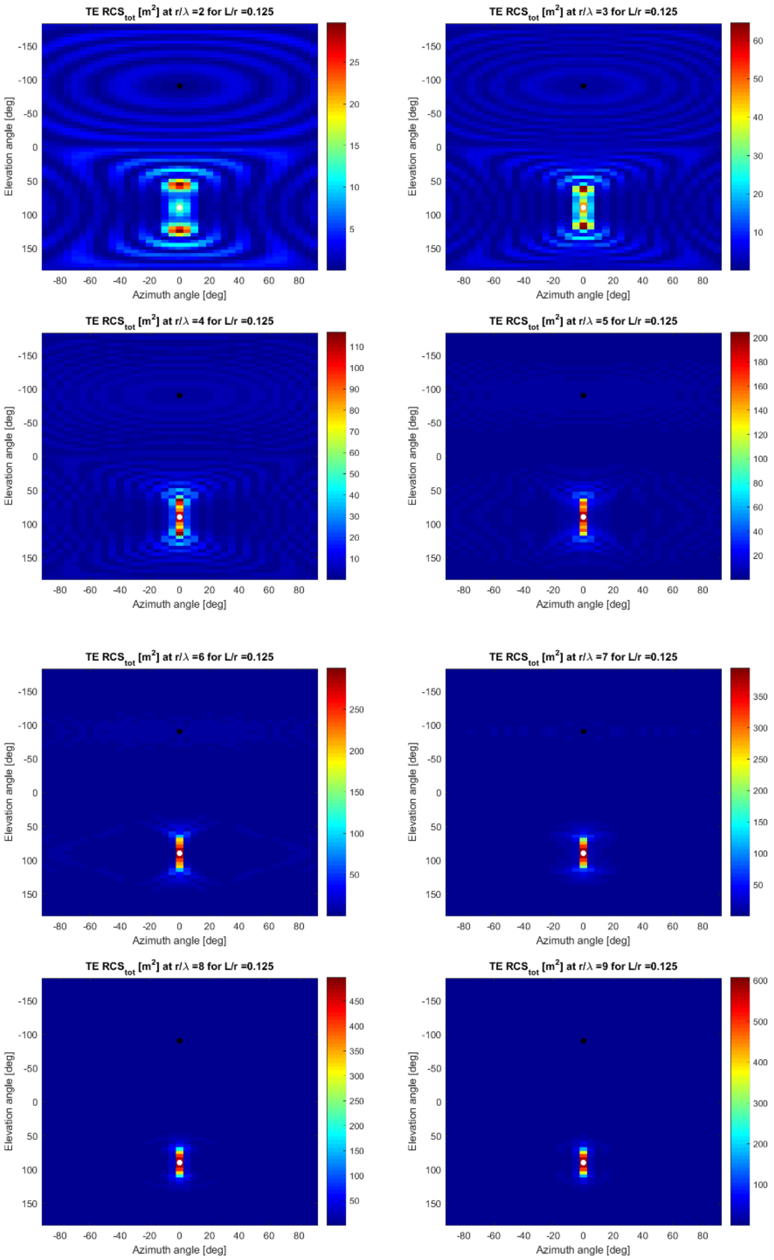

Figure 12a. Total RCS map of a cylinder (L = 37.5 cm, L/2r = 0.0625) illuminated at (φ, θ) = (0^0, 90^0) with a TE-polarized plane wave (black dot – the backward-scattering angle, white dot – the forward-scattering angle).

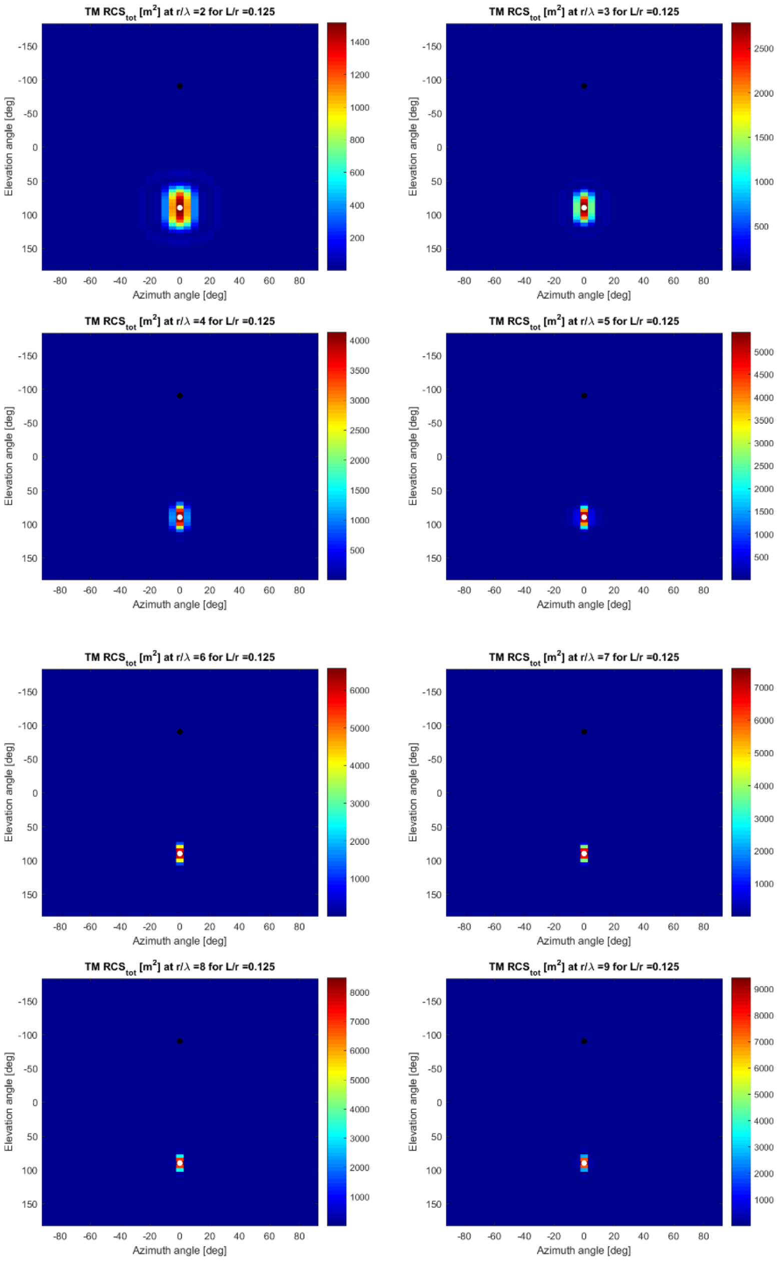

Figure 12b. Total RCS map of a cylinder (L = 37.5 cm, L/2r = 0.0625) illuminated at (φ, θ) = (0^0, 90^0) with a TM-polarized plane wave (black dot – the backward-scattering angle, white dot – the forward-scattering angle).

4.3 A Metallic Plate

In this section, a rectangular metallic plate (*a* x *b*) oriented in the xy-plane is considered. It can be noticed in Figure 13 that side illumination of a small square metallic plate with a TE-polarized plane wave results in the forward scattering relatively small at both small and high frequencies. The outcome differs in case of applying TM polarization which results in the forward scattering substantially enhanced at high frequencies. Moreover, the scattering of a TM plane wave is at least one order of magnitude larger (compare Figure 13A and 13B). Subsequently, the normal illumination of the small square metallic plate results in the forward scattering increasing with the frequency for both polarizations.

As the aspect ratio, a/b, is increasing, the side illumination with high frequencies at a longer side of the plate results in a significant enhancement of the forward scattering at higher order angles which are shaped in the angular domain into scattering circles with a minimum (a maximum) at the forward scattering angle of TE (TM) polarization.

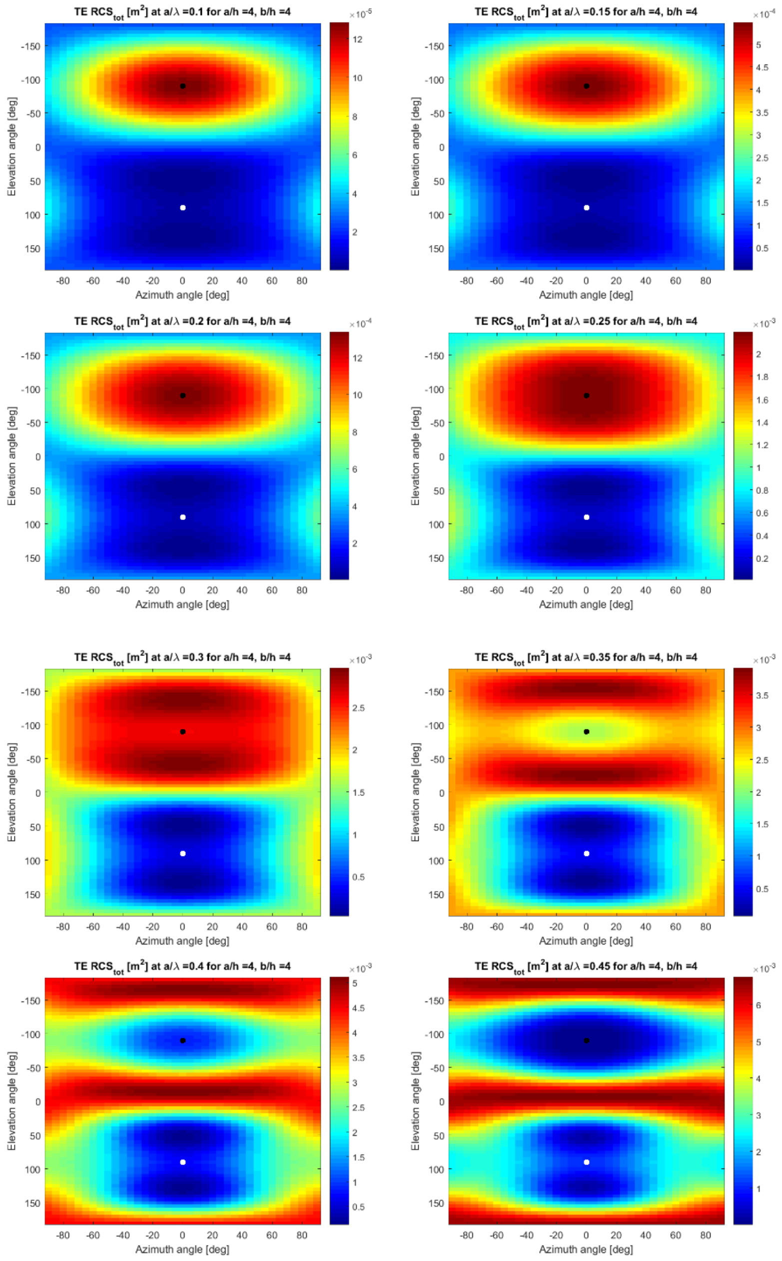

Figure 13A. Total RCS map of a plate (h = 3.75 cm, a/h = 4, b/h = 4) illuminated at (φ, θ) = (0^0, 90^0) with a TE-polarized plane wave (black dot – the backward-scattering angle, white dot – the forward-scattering angle).

This material is based upon work supported by the Air Force Office of Scientific Research, Air Force Material Command, USAF under Award No. FA9550-17-1-0041.

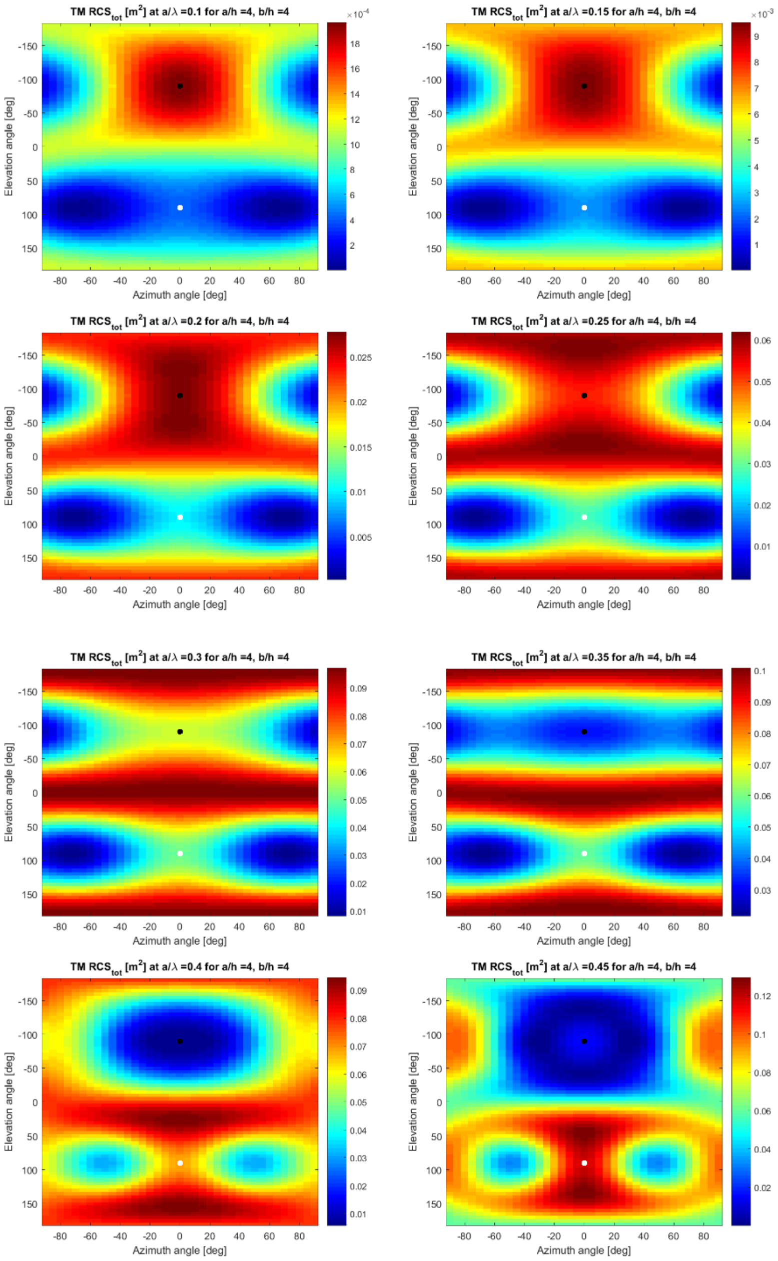

TM RCS$_{tot}$ [m^2] at a/λ =0.1 for a/h =4, b/h =4

TM RCS$_{tot}$ [m^2] at a/λ =0.15 for a/h =4, b/h =4

TM RCS$_{tot}$ [m^2] at a/λ =0.2 for a/h =4, b/h =4

TM RCS$_{tot}$ [m^2] at a/λ =0.25 for a/h =4, b/h =4

TM RCS$_{tot}$ [m^2] at a/λ =0.3 for a/h =4, b/h =4

TM RCS$_{tot}$ [m^2] at a/λ =0.35 for a/h =4, b/h =4

TM RCS$_{tot}$ [m^2] at a/λ =0.4 for a/h =4, b/h =4

TM RCS$_{tot}$ [m^2] at a/λ =0.45 for a/h =4, b/h =4

Figure 13B. Total RCS map of a plate (h = 3.75 cm, a/h = 4, b/h = 4) illuminated at (φ, θ) = (0^0, 90^0) with a TM-polarized plane wave (black dot – the backward-scattering angle, white dot – the forward-scattering angle).

5. Theoretical RCS Analysis

An attempt of carrying out an analytical study of the scattering of a plane wave from metallic objects of the canonical shapes at higher frequencies can also be undertaken using techniques known in the literature [8]. The corresponding theories are usually based on the surface equivalent theorem (derived from the Huygens principle), which states that EM field in a lossy medium is uniquely specified by the sources within the considered region supplemented with either tangential components of the electric field over the boundary or tangential components of the magnetic field over the boundary or the former over a part of the boundary and the latter over the rest of the boundary [9]. That concept is exemplified in Figure 14, where the actual problem with the radiating electric (J_1) and magnetic (M_1) sources is replaced with a problem without both radiating sources within the considered volume, but with new equivalent sources (J_s, M_s) applied at the surface splitting the volume. Those new current densities are equivalent only in the outer volume, where they are expected to reproduce the original fields (E_1, H_1) correctly. Since virtually anything can become the internal fields (E,H) in the equivalent problem, it can be assumed – as simplification – that they are zero, which is known as the *Love's equivalent principle*:

$$\vec{J}_S = \hat{n} \times \vec{H}_1 \tag{9}$$

$$\vec{M}_S = -\hat{n} \times \vec{E}_1 \tag{10}$$

As the aforementioned surface equivalent theorem allows neglecting one of the currents, the resulting equivalent problems may be depicted by Figure 15, with one of the currents, magnetic or electric, specified on the electric conductor or magnetic one, respectively. However, a major difficulty in applying one of these equivalent problems is that the current densities do not radiate into an unbounded medium with the well-known Green's function.

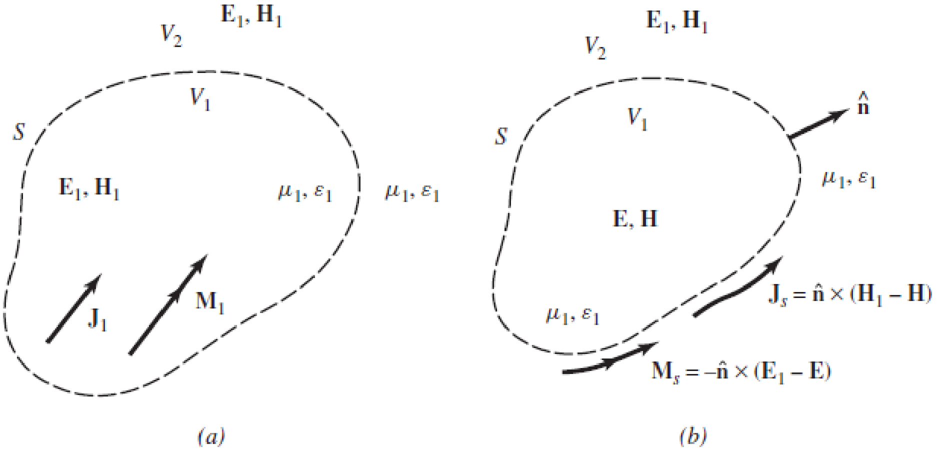

Figure 14. (a) Actual and (b) equivalent problems [8].

This material is based upon work supported by the Air Force Office of Scientific Research, Air Force Material Command, USAF under Award No. FA9550-17-1-0041.

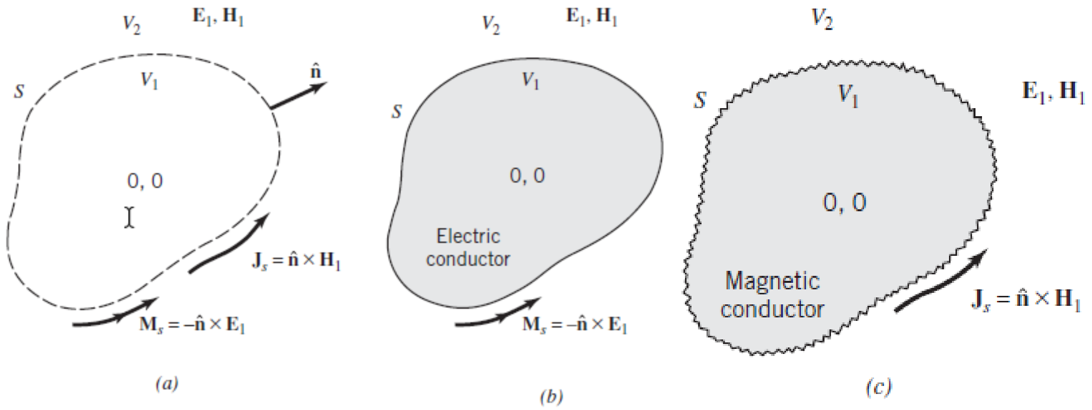

Figure 15. (a) Love's equivalent. (b) Electric conductor equivalent. (c) Magnetic conductor equivalent [8].

That difficulty can be conditionally overcome if one assumes that the surface of the conductor is flat and it extends to infinity. In such case, the image theory can be applied, which allows replacing the current located at the conducting surface with the equivalent free space problem (see Figure 16).

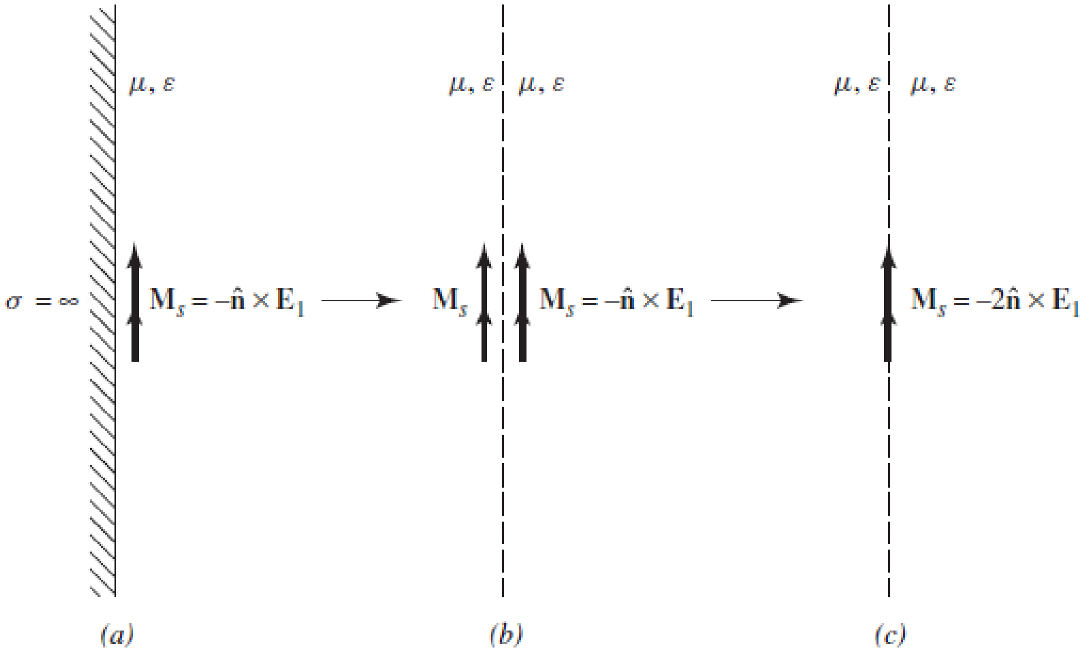

Figure 16. Equivalent model of the radiation of a magnetic source near flat perfectly conducting surface [8].

This material is based upon work supported by the Air Force Office of Scientific Research, Air Force Material Command, USAF under Award No. FA9550-17-1-0041.

5.1. Induction Equivalent

Once the basic principles of the surface equivalence theorem are briefly introduced, let us extend its applicability to the scattering phenomenon, where the radiating current sources (J_1, M_1) are now specified outside a given volume called an obstacle as shown in Figure 17 (compare Figure 14). The total field outside the given volume of the obstacle consists of the original field in the absence of the obstacle (E_1, H_1) and the field scattered by the obstacle (E_s, H_s):

$$\vec{E} = \vec{E}_1 + \vec{E}_S \tag{11}$$

$$\vec{H} = \vec{H}_1 + \vec{H}_S \tag{12}$$

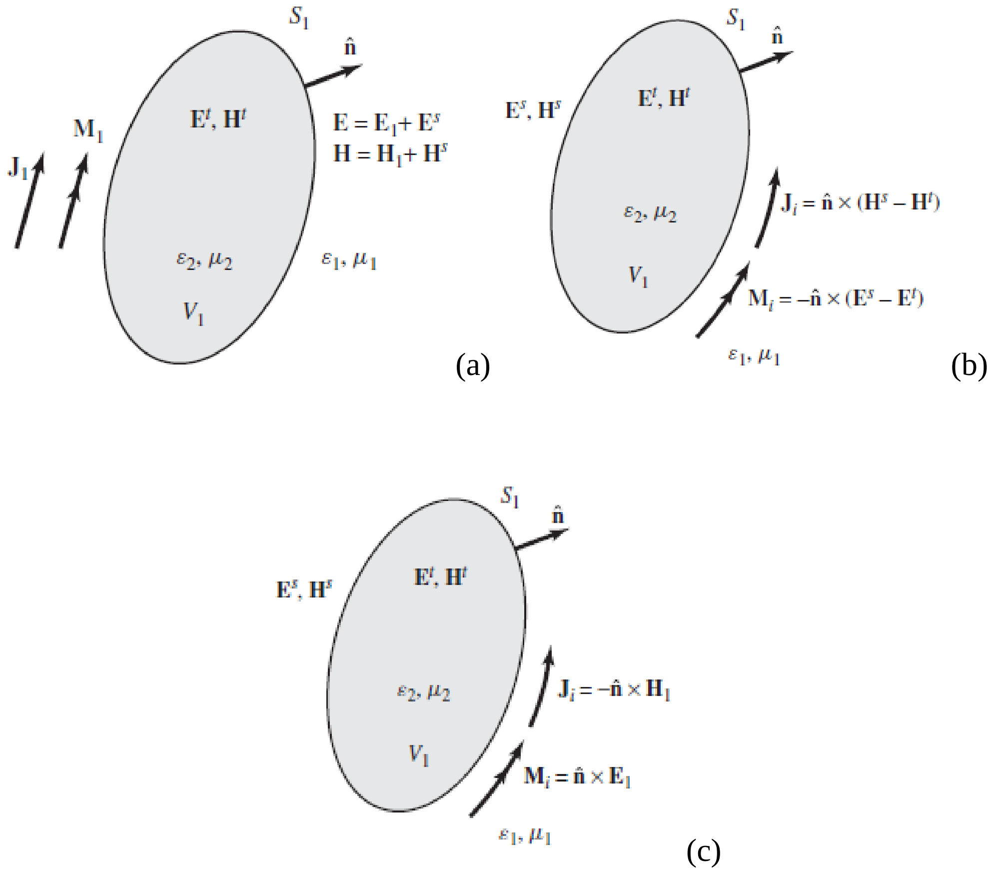

Figure 17. Induction equivalent [8].

In order to find the scattered fields (E_s, H_s), the problem shown in Figure 17a can be formulated in the alternative form shown in Figure 17b. Radiating currents (J_1, M_1) are missing and the outer field consists of only scattered components as the incident ones do not contribute to the scattering. To support such fields, equivalent current densities (J_i, M_i) are introduced on the boundary. Applying appropriate boundary conditions, the model can be further reduced to the one shown in Figure 17c, where the equivalent surface currents are given as a function of the known incident fields. The equivalent problem shown in Figure 17c, known as an **induction equivalent**, is of the same difficulty as the original one as two media are still present.

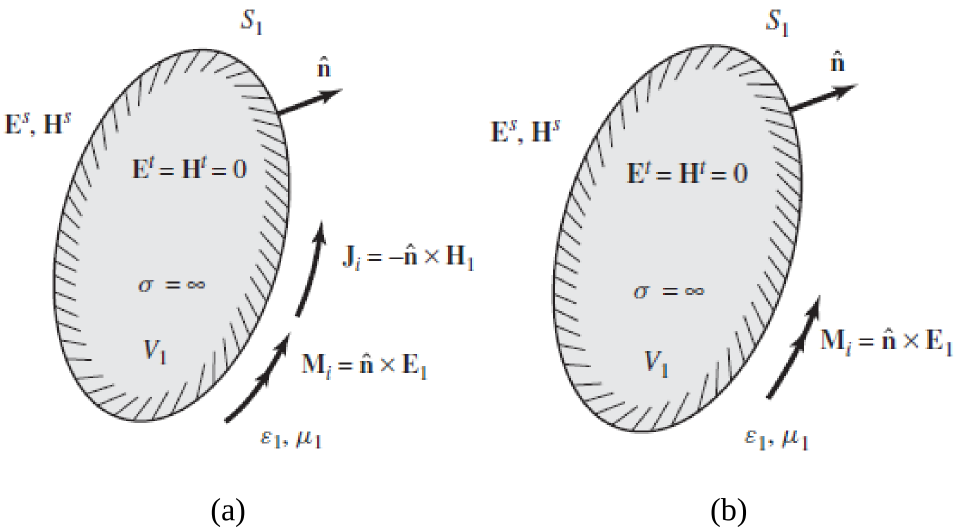

Figure 18. Induction equivalents for PEC scattering [8].

Consider now the obstacle made of a perfect electric conductor (PEC). In that case, Figure 17c changes to Figure 18a. However, the uniqueness theorem allows neglecting one of the currents. Consequently, if the magnetic current density M_i is considered only, Figure 18a reduces to that of Figure 18b, which is known as an **induction equivalent for PEC**. When the surface is of a complex shape, the exact solution to the equivalent problem of Figure 18b is not easier to compute than the solution to the original one. On the contrary, if the surface is flat the problem can be solved approximately by applying the aforementioned image theory, which leads to the following magnetic current located in free space:

$$\vec{M}_S = \hat{n} \times \vec{E}_1 + \hat{n} \times \vec{E}_1 = \mathbf{2}\,\hat{\boldsymbol{n}} \times \vec{\boldsymbol{E}}_{\mathbf{1}} \tag{13}$$

5.2. Physical Equivalent

An alternative formulation for the PEC scattering is known as a **physical equivalent**. In that approach, boundary conditions are used in a straightforward manner to conclude that the magnetic current is suppressed at the PEC surface, while the electric current is related to the total tangential component of the magnetic field H:

$$\vec{M}_S = -\hat{n} \times \vec{E} = 0 \tag{14}$$

$$\vec{J}_S = \hat{n} \times \vec{H} \tag{15}$$

These relations can be rearranged as follows:

This material is based upon work supported by the Air Force Office of Scientific Research, Air Force Material Command, USAF under Award No. FA9550-17-1-0041.

$$\vec{M}_S = -\hat{n} \times \vec{E} = -\hat{n} \times \left(\vec{E}_S + \vec{E}_1\right) = -\hat{n} \times \left[\vec{E}_S - \left(-\vec{E}_1\right)\right] \tag{16}$$

$$\vec{J}_S = \hat{n} \times \vec{H} = \hat{n} \times \left(\vec{H}_S + \vec{H}_1\right) = \hat{n} \times \left[\vec{H}_S - \left(-\vec{H}_1\right)\right] \tag{17}$$

which show that the original problem with PEC inside the considered volume can be replaced with that shown in Figure 19 with the same medium in both regions.

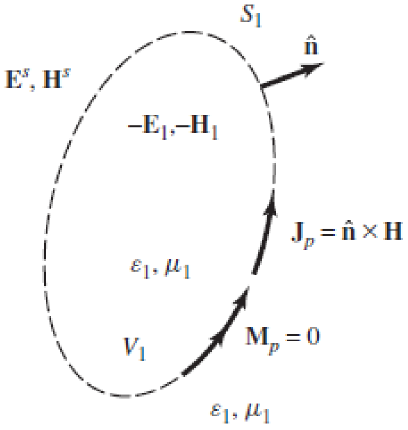

Figure 19. Physical equivalent for PEC scattering [8].

The advantage of the physical equivalent is that the problem is now specified in a single medium, so well-known relations for the radiation in the unbounded free-space can be used to calculate the scattered field in the far field zone. Unfortunately, the total magnetic field H is not known a priori, which means that the scenario shown in Figure 19 is not, in general, simpler than the original one. However, if the conducting obstacle is flat the image theory can be applied leading to the **physical optics** approximation:

$$\vec{J}_S = \hat{n} \times \vec{H} = \hat{n} \times \left(\vec{H}_S + \vec{H}_1\right) = \mathbf{2}\,\hat{\boldsymbol{n}} \times \vec{\boldsymbol{H}}_{\mathbf{1}} \tag{18}$$

Practically, Eq. (7) and (12) can be used to obtain the equivalent currents at those regions of the object, which are directly illuminated with the wave, while in the shadow region the equivalent current density is set to zero.

5.3. Scattered Fields

Electromagnetic fields in the far-field zone can be computed solving the following differential formulae:

$$\nabla^2\vec{A} + \beta^2\vec{A} = -\mu\vec{J} \tag{19}$$

$$\nabla^2\vec{F} + \beta^2\vec{F} = -\varepsilon\vec{M} \tag{20}$$

where A and F are magnetic and electric vector potentials, respectively. The solution of Eq. (19) and (20) is as follows:

$$\vec{A} = \frac{\mu}{4\pi} \iiint_V \vec{J}(\vec{r}') \frac{e^{-j\beta R}}{R} dv' \tag{21}$$

$$\vec{F} = \frac{\varepsilon}{4\pi} \iiint_V \vec{M}(\vec{r}') \frac{e^{-j\beta R}}{R} dv' \tag{22}$$

where R is the source to the observation distance.

Eventually, the EM fields can be calculated as follows:

$$\vec{H}_A = \frac{1}{\mu} \nabla \times \vec{A} \tag{23}$$

$$\vec{E}_A = \frac{1}{j\omega\varepsilon} \nabla \times \vec{H}_A \tag{24}$$

$$\vec{E}_F = -\frac{1}{\varepsilon} \nabla \times \vec{F} \tag{25}$$

$$\vec{H}_F = -\frac{1}{j\omega\mu} \nabla \times \vec{E}_F \tag{26}$$

$$\vec{H} = \vec{H}_A + \vec{H}_F \tag{27}$$

$$\vec{E} = \vec{E}_A + \vec{E}_F \tag{28}$$

Consider as an example a square plate made of perfect electric conductor (h = 3.75 cm, a = 5λ, b = 5λ) illuminated at (φ, θ) = (0^0, 150^0) with a TM-polarized plane wave. Figure 20 shows calculations made using a physical optics approximation, the induction theorem, analytical formulae [8] and the FDTD method. It can be noticed that decent agreement has been obtained at the back-scattering angle. Large similarity between the physical optics approximation and the induction theorem indicates that there is no special difference in the choice of electric or magnetic currents to the modeling of equivalent currents in the theory presented above.

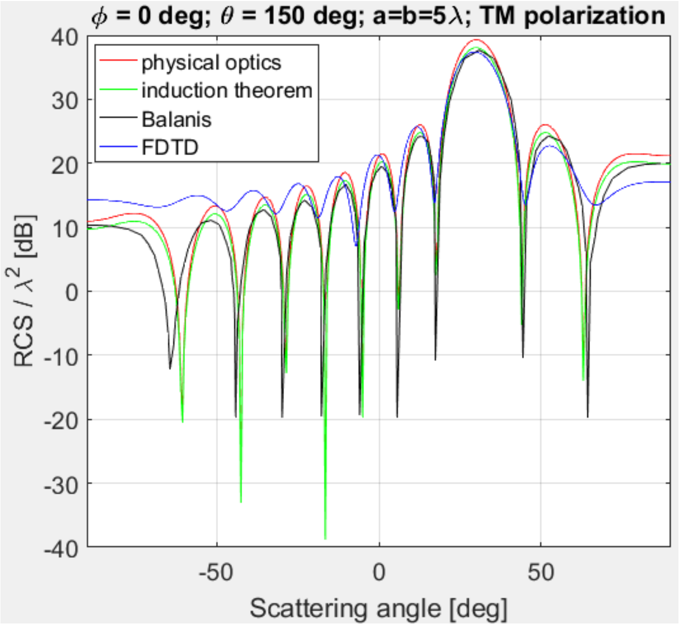

Figure 20. RCS of a square plate made of perfect electric conductor (h = 3.75 cm, a = 5λ, b = 5λ) illuminated at (φ, θ) = (0^0, 150^0) with a TM-polarized plane wave calculated with various methods.

This material is based upon work supported by the Air Force Office of Scientific Research, Air Force Material Command, USAF under Award No. FA9550-17-1-0041.

6. Literature

[1] H. G. Booker. Slot aerials and their relation to complementary wire aerials (Babinet’s principle). Journal of the Institution of Electrical Engineers - Part IIIA: Radiolocation, 93(4):620–626, 1946.

[2] Mikhail Cherniakov. Bistatic Radar: Principles and Practice. Bistatic Radar: Principles and Practice, pages 1–504, May 2007.

[3] Siegel, K.M. Bistatic radar cross sections of surfaces of revolution. Journal of Applied Physics, 26(1):297–305, 1955.

[4] Nicholas J. Willis. Bistatic Radar. SciTech Publishing, 2005.

[5] H. Griffiths and N. Willis, „Klein Heidelberg–a WW2 bistatic radar system that was decades ahead of its time”, lis. 2017.

[6] M. Gashinova, L. Daniel, K. Kabakchiev, V. Sizov, E. Hoare, i M. Cherniakov, „Phenomenology of signals in FSR for surface targets detection”, w IET International Conference on Radar Systems (Radar 2012), 2012, s. 1–6.

[7] QuickWave-3D (QW-3D) electromagnetic simulator.

[8] C. A. Balanis, *Advanced Engineering Electromagnetics*, John Wiley & Sons, Inc.

[9] R. F. Harrington, *Time-Harmonic Electromagnetic Fields*, McGraw-Hill, New York, 1961.